Effect of Defects on Fatigue Strength of GTAW Repaired Cast Aluminum Alloy

Fatigue test data were analyzed to determine the relationship between defects and fatigue performance of weld repaired aluminum castings

BY L. LI, Z. LIU, AND M. SNOW

ABSTRACT. The effect of porosity on the fatigue life of weld repaired D357 aluminum cast alloy was investigated. Investment cast D357 aluminum alloy was repaired with gas tungsten arc (GTA) welding using a matching filler metal. The repaired alloy underwent a postweld heat treatment involving solutioning and artificial aging. The number of cycles to failure of the welded specimens showed a much wider distribution band than those of the as-cast specimens. Crack-like shrinkage porosity was identified to be the predominant factor leading to the inconsistent fatigue strength of the welded specimens. The relationship between defects in the fusion zone and fatigue failure cycles was statistically analyzed. Crack-like shrinkage porosity in the welds was found to have the most significant effect in decreasing the fatigue life of the welded specimens. Spherical pores also contributed to decreasing the fatigue life of welded specimens, although not as significant as the crack-like pores.

Introduction

Welding repair is occasionally a necessary process in fabrication of cast aluminum structures. Properly repaired aluminum castings may have equivalent static strength, ductility, fracture toughness, and fatigue strength levels as the as-cast structures. For cast structures designed to be used for aerospace applications, fatigue property is a critical performance parameter. Past experience and published literature on this issue indicate that casting defects (cracking, porosity, inclusions) and microstructure (coarse second phases) decrease the fatigue strength of aluminum castings (Refs. 1–4). Welding and weld repair may introduce further complications due to not only additional metallurgical defects, but also geometric discontinuity and residual stresses (Refs. 5, 6). Some researchers advised against repair welding (Ref. 7), citing the possibility of additional residual stresses and defects. Some researchers suggest a tighter control of defect sizes. For instance, Nordmark et al. (Ref. 5) suggested that incomplete fusion and porosity in the repair welds did not lower the fatigue strength if the defects were smaller than a certain size. While ways to avoid weld cracking and porosity defects have been actively investigated (Refs. 8–10), remedial methods to increase the weld fatigue strength are widely used. Shot peening and heat treating (Ref. 11) have been used to increase the fatigue properties of welded aluminum joints.

The causes for the degraded fatigue property in an industrial setting can be many and complicated, ranging from base materials composition, melting and casting procedures, heat treatment, weld repair procedures, and quality control process. This study reports an attempt to analyze and interpret more than 200 sets of fatigue testing data, gathered over two years from as-cast and weld repaired D357 alloy, in order to find out the relationship between defects and the fatigue performance of weld-repaired D357 aluminum castings.

KEYWORDS

Aluminum Casting
Weld Fatigue
Repair Weld
Weld Defects

L. LI is an assistant professor in the Department of Mechanical and Aerospace Engineering at Utah State University, Logan, Utah. Z. LIU is a visiting researcher from Zhengzhou University, China. M. SNOW is a metallurgical engineer with GSC Foundries Inc., Ogden, Utah.

Experimental Procedure

Specimens for fatigue tests were prepared as part of the actual investment casting of D357 aluminum alloy, as specified by the aerospace material specification AMS 4249, with the nominal composition (in wt-%) of Si 6.50–7.50, Mg 0.55–0.60, Ti 0.10–0.20, Be 0.04–0.07, Fe 0–0.12, Mn 0–0.10, Al balance. The fatigue specimens were cut from the castings and underwent a simulated repair welding. The welding was done with the manual gas tungsten arc (GTA) spot welding process, for simulating the repair of casting defects during the actual production. The welding filler metal, 1.575-mm- (0.062-in.-) diameter R-357 specified by AWS A5.10-99, was of the same nominal composition of the casting alloy except that the welding filler metal did not contain Be. The welding current was 22 A for the spot welding on the 3.175-mm (⅛- in.-) thick specimens, with the current ratio of direct current electrode negative (DCEN) to direct current electrode positive (DCEP) set to 5.9:1, with a frequency of variable polarity of 50 Hz. A gas mixture of 24% Ar, 76% He was used for the arc and pure (99.998%) Ar was used for back shielding. A total of 150 s of welding was conducted on a spot. Approximately 110 s of welding was conducted on the front side of the sample. The sample was flipped over, and about 40 s of welding was conducted on the backside of the sample. Following welding, the welded area was ground flush with the base metal. Heat treating for both the as-cast specimens and weld-repaired specimens involved a 549°C (1020°F) solution treatment (72 h with Glycol quench) followed by 171°C (340°F) aging (5.5 h with air cooling).

The geometry and dimensions of the fatigue specimen were designed according to ASTM E 466 with a 2.54-mm- (0.1-in.-) diameter though-hole machined at the center of the weld spot that was located at the center of the specimen — Fig. 1. The

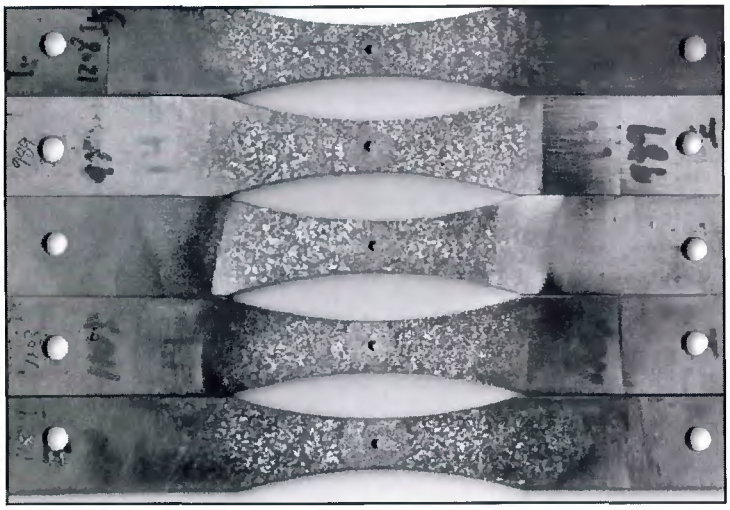

Fig. 1 — Fatigue test specimens of GTA welding repaired D357 alloy. A stress-concentration hole is located at the center of the weld. Specimens were etched after fatigue testing to show the location of welds and the grain size.

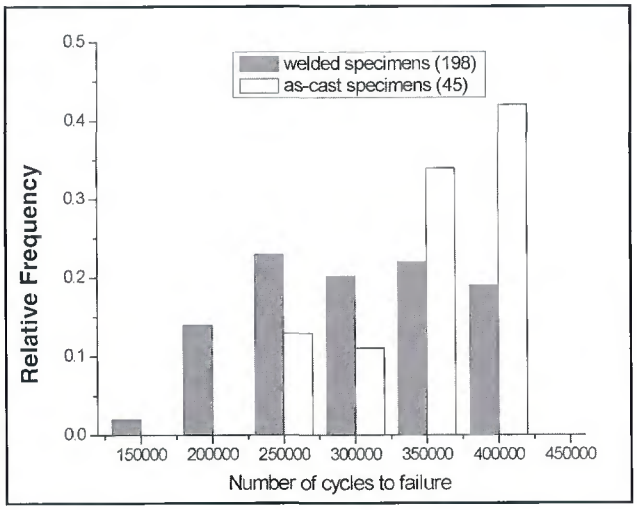

Fig. 2 — Distribution of fatigue failure cycles for 198 repair-welded specimens and 45 as-cast specimens.

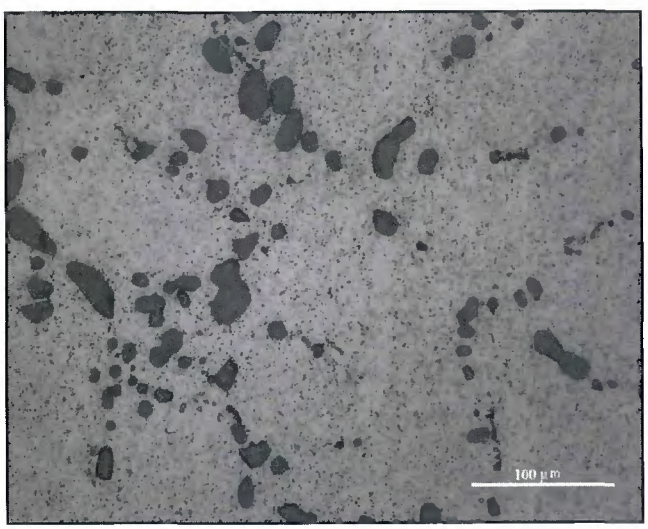

Fig. 3 — Microstructure of the base material following solutioning and aging.

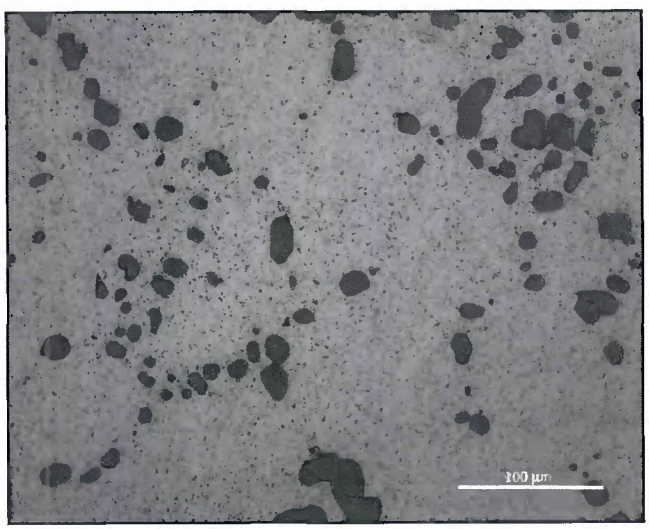

Fig. 4 — Microstructure of the fusion zone following solutioning and aging.

specimen has a thickness of 3.175 mm (⅛ in.), with either the as invest-cast surface finish for the cast specimens, or the ground surface finish for the weld-repaired specimens. The fatigue testing was conducted in accordance with ASTM E 466 at a loading frequency of 15 Hz. The maximum stress was 103.4 MPa (15 ksi) at a stress ratio of 0.1 and stress concentration factor of 2.5. The average fatigue life was recorded. The fatigue tests were stopped at 400,000 cycles if the specimens had not failed. A total of 198 weld-repaired specimens and 45 as-cast specimens were tested in this study.

All fatigue-tested specimens were analyzed with a stereographic binocular microscope. The macroscopic observation provided information on bulk behavior of the specimens, including the existence of defects, degree of plastic deformation, origin of the fatigue crack and propagation path. Digital images were taken and recorded for further analysis. Following the macroscopic analysis, specimens were mounted in the longitudinal orientation of fatigue-tested specimens, and prepared for microscopic observation. The microstructure was recorded using the PaX-IT™ digital imaging system mounted on a Zeiss metallurgical microscope. The mounted and fractured specimens were observed under a Hitachi scanning electron microscope. The quantitative analysis of porosity in the welds was conducted on samples in the as-polished condition (without etching). For microstructure observation, the specimens were etched with 2% HF in water. Digital images of the entire weld area of each sample were captured under the microscope at 350× magnification. An image-processing software was used to measure the size, shape, and area fraction of the porosity. Statistical methods were used to process the measured data.

Results

Fatigue failure cycles of weld-repaired and as-cast specimens in the heat-treated condition are shown in Fig. 2. The weld-repaired specimens exhibited a much wider distribution of fatigue cycles than

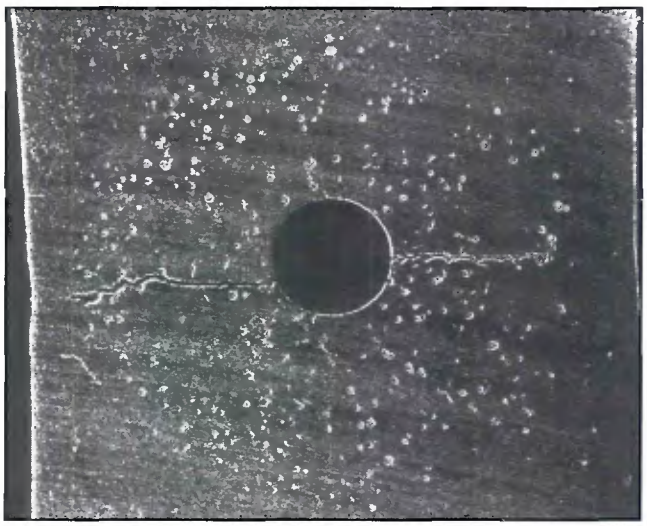

Fig. 5 — The as-polished surface of a typical sample with low fatigue cycle. Shrinkage porosity is observed in the weld zone.

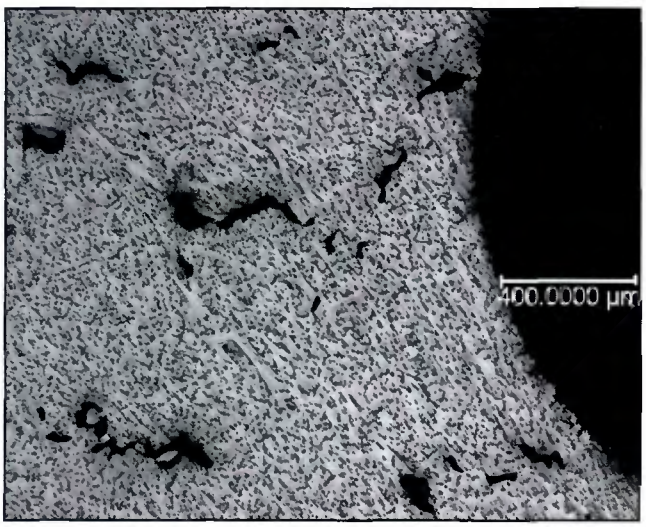

Fig. 6 — Crack-like shrinkage porosity with the length/width ratio of 0.1397/0.0396 near the weld center, where the stress-concentration hole (right of the photomicrograph) is located.

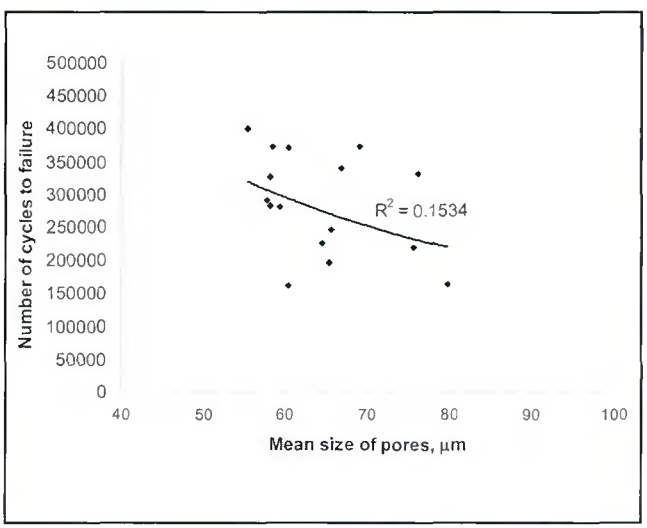

Fig. 7 — Fatigue failure cycles as a function of mean size of pores in welds.

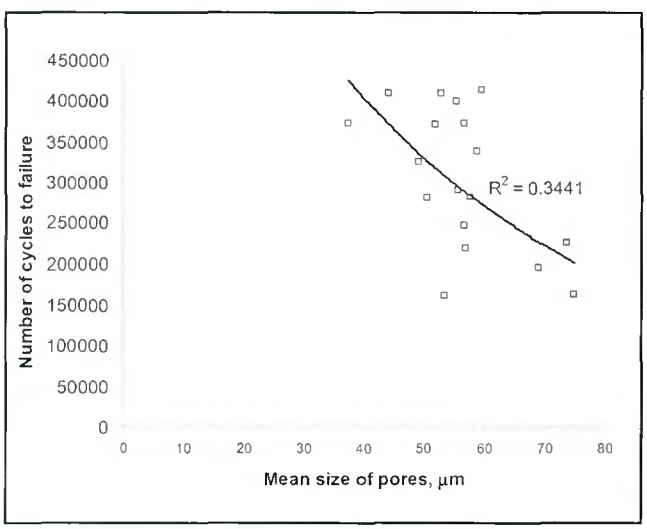

Fig. 8 — Fatigue failure cycles as a function of mean size of pores in the 0.5-mm-thick ring-shaped region around the stress-concentration hole.

the as-cast specimens. About 20% of the welded specimens had achieved 400,000 fatigue cycles, and there were about 20% of the welded specimens to have less than 200,000 fatigue cycles. The remaining welded specimens were approximately evenly distributed between 250,000 and 350,000 fatigue cycles. In comparison, all of the as-cast specimens had fatigue failure cycles greater than 250,000, and about 45% of the as-cast specimens had fatigue cycles no less than 400,000.

The microstructure of the base material following solutioning and aging is shown in Fig. 3. The rounded, dark gray, Si particles are distributed along the grain boundaries, while smaller precipitates are dispersed intragranularly upon the aging treatment. The microstructure of weld-repaired specimens, shown in Fig. 4, is almost the same as the cast specimens, except the grain size for the weld is smaller. Specimens with high fatigue failure cycles generally had some common features, including the fine-grain-sized microstructure in the weld fusion zone, the shape of the grains was nearly equiaxed following heat treatment; and, most importantly, there were no significant crack-like porosity defects.

Specimens with low-fatigue failure cycles invariably contained different levels of defects. The predominant defect was porosity in the weld fusion zone, as shown in Fig. 5 for a severe case. The fatigue fracture originated from the stress-concentration hole at the center of the weld, propagated in both directions perpendicular to the longitudinal axis (the fatigue loading direction) of the sample. Some specimens fractured completely and some specimens fractured partially, in which case the fatigue cracking was constrained within the weld fusion zone, i.e., the cracking was arrested at the weld boundary. Crack-like voids were generally found near the center of the weld (Fig. 6), while the spherical pores tend to be distributed over the entire weld.

Measurements of spherical porosity and crack-like porosity from the fatigue-tested samples confirmed quantitatively the above observations. These measurements are presented here in the order of

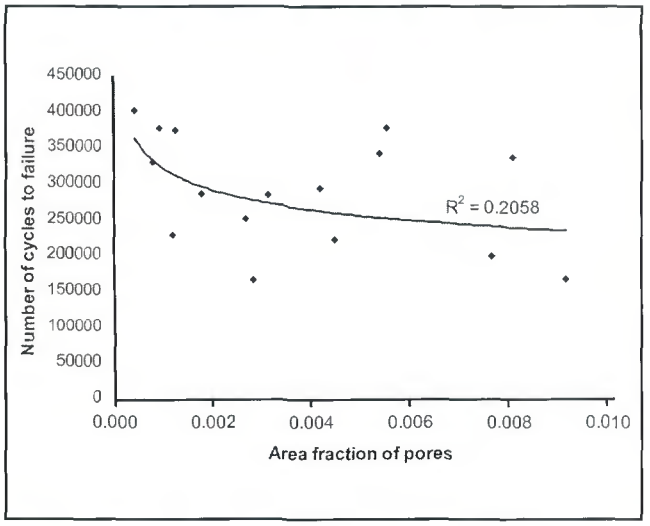

Fig. 9 — Fatigue failure cycles as a function of the area fraction of pores in welds.

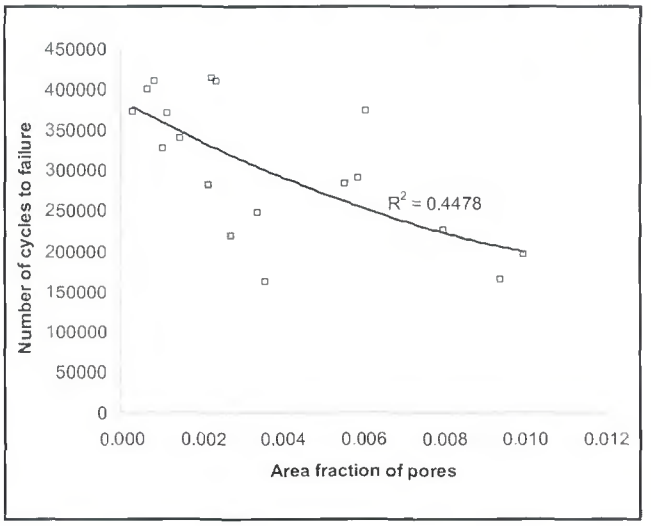

Fig. 10 — Fatigue failure cycles as a function of the area fraction of pores in the 0.5-mm-thick ring-shaped region around the stress-concentration hole.

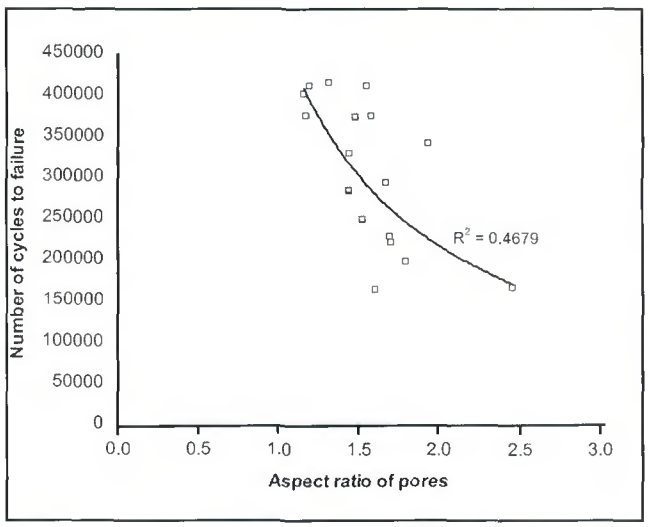

Fig. 11 — Fatigue failure cycles as a function of the aspect ratio of pores in the 0.5-mm-thick ring-shaped region around the stress-concentration hole.

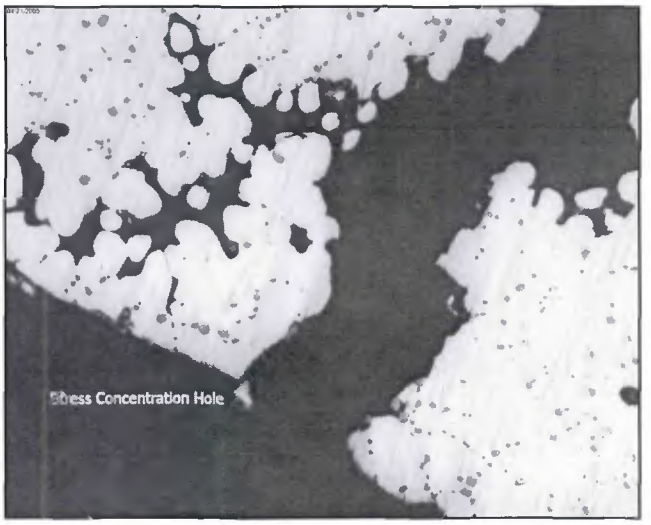

Fig. 12 — The role of crack-like shrinkage porosity in fatigue cracking initiation and propagation. The stress-concentration hole is shown at the lower left of the micrograph.

mean size, total amount, and shape (aspect ratio of length to width) of the porosity defects. The distinction between the spherical and crack-like pores was represented by the shape (aspect ratio). It was observed that the variation from spherical pores to microcracks was almost continuous, making it difficult to clearly define a microcrack. Therefore, for the statistical analysis, the term "pores" is used to include both the spherical and crack-like pores.

Figure 7 shows the fatigue failure cycles as influenced by the mean size of pores in the welded specimens. With much scatter, a weak correlation (R^2 = 0.153) was observed between the fatigue failure cycles and the mean size of pores. The general trend was that the greater the mean size of pores, the lower the fatigue cycles. It was believed that pores that were distributed near the region where the fatigue crack initiated should have more significant effects on the fatigue life (Ref. 2). When the pores that were distributed within a ring of 500 μm around the stress-concentration hole were counted, the mean size indicated a more obvious correlation (R^2 = 0.344) with the failure cycles — Fig. 8. The increased correlation confirmed the more significant effect of pores at the fatigue initiation sites. For the samples with lower fatigue cycles, the mean size of pores was up to about 75 μm; for the samples with higher fatigue cycles, the mean size of pores was within a 40 to 60 μm range.

The total amount of porosity in terms of the area fraction of pores, defined as ratio of the area of pores to the area of weld, was plotted against fatigue failure cycles — Fig. 9. The scatter of data was still significant, with the correlation factor R^2 = 0.206 between the area fraction of pores and the fatigue cycles. It seems the total amount of porosity in welds had a similar, but more pronounced effect on fatigue cycles than the mean size of pores in

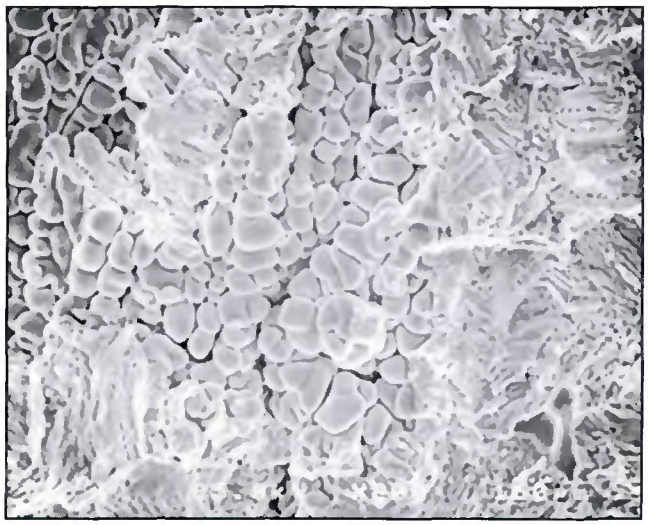

Fig. 13 — Fracture surface of a crack-like shrinkage porosity, showing dendrite surfaces.

Fig. 14 — Fractography of a porosity-containing, fatigue-tested specimen.

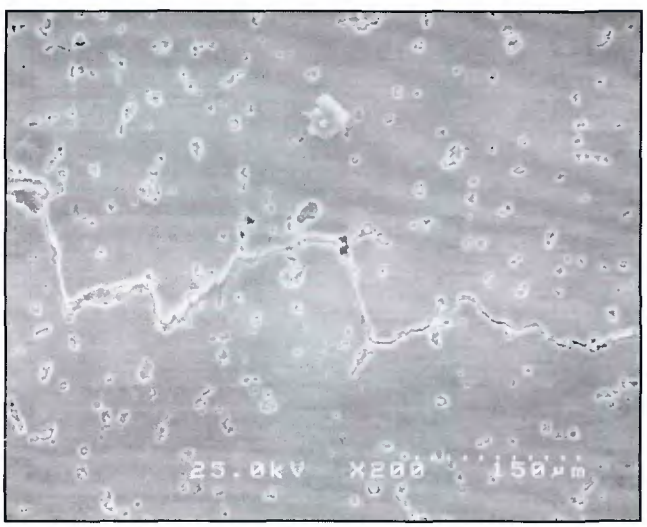

Fig. 15 — Fatigue crack propagation along the grain/interdendritic boundaries in the weld fusion zone. The Si-rich particles are distributed at the grain/interdendritic boundaries.

Fig. 16 — Magnified region A in Fig. 14. The fracture mechanism appears to be microvoid coalescence (dimples) along the grain/interdendritic boundaries.

welds. When the pores that were distributed within a ring of 500 μm around the stress-concentration hole were counted, the amount of porosity showed a more definite correlation (R^2 = 0.448) to the number of cycles to failure — Fig. 10. For the samples with 400,000 failure cycles, the area faction of porosity was lower than 0.001. For the samples with failure cycles lower than 200,000, the area fraction of porosity was higher than 0.008.

The shapes of porosity defects ranged from spherical pores to elongated shrinkage cavities and cracks. To describe the shape of these porous defects, the average aspect ratio of length to width was measured from the tested specimens. The plot of fatigue cycles against the aspect ratio for the pores that were distributed within a ring of 500 μm around the stress-concentration hole showed a clear trend: the higher the aspect ratio (or the more "crack-like" for the pore shape), the lower the fatigue cycles. Specimens with high fatigue cycles generally contained pores that were more spherical, with the aspect ratio less than 1.5 — Fig. 11.

All the above statistical data seemed to indicate that the amount and shape of the porosity near the stress-concentration hole had a greater effect on the failure cycles than the porosity distributed in other areas of the weld. This observation confirmed the role of defects close to the surface on decreasing the fatigue life, as observed in other studies (Refs. 2, 12). Among the parameters that describe the porosity defects, the aspect ratio seemed to have the highest degree of correlation to fatigue life, indicating the crack-like defects to be more potent in decreasing the fatigue life. The amount of porosity, measured by fraction of porosity area, seemed to have the second-highest degree of correlation with fatigue life. The average size of the porosity seemed to have the least degree of correlation to fatigue life. Apparently, the probability for a porosity to

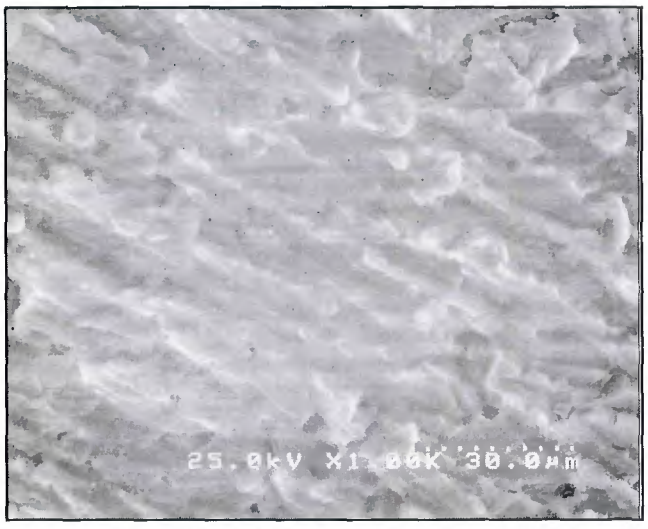

Fig. 17 — Magnified region B in Fig. 14. Fatigue striations are clearly seen.

be right at the crack initiation site was mainly determined by the amount of porosity.

Discussion

The existence of crack-like porosity exposed to the stress-concentration hole, which was located near the center of the weld, might have provided the initiation sites for the fatigue failure. An example of such accelerated formation of fatigue fracture is shown in Fig. 12. Welded specimens that showed the lowest fatigue cycles almost always contained a significant amount of crack-like porosity. The fracture surface of a typical crack-like pore is shown in Fig. 13. Dendritic features and shrinkage cavities indicated a typical solidification hot cracking mechanism for the formation of the crack-like porosity. Having a crack-like geometry, and a minute crack tip radius, these pores effectively acted as preformed fatigue cracks. Consequently, there was an absence of crack nucleation period, explaining the premature fatigue failure for the specimens containing crack-like porosity.

Porosity defects in the repair welds also accelerated the fatigue crack propagation. An example is shown in Fig. 14, in which the fatigue crack is seen to have propagated through the pores as a low-resistance path. The fatigue crack propagated intergranularly along the grain/interdendritic boundaries that are delineated by silicon particles — Fig. 15. The propagation connected the pores and bypassed or cut through the silicon particles, which were dispersed in the interdendritic boundaries. The fracture surfaces revealed micromechanisms for the fatigue failure. The separation was mostly through the "dimple" or micro microvoid coalescence along the grain/interdendritic boundaries — Fig. 16. Because of the existence of defects, the specimens did not fail by typical fatigue failure mechanism, but rather by a fast fracture mechanism. In areas that are free of defects, small regions created by a typical fatigue failure mechanism could be seen. In Fig. 17, the fatigue striations and transgranular propagation path are clearly visible. It seems the fatigue specimens tested in this study involved a mixed fracture mechanism: fast fracture around defects and fatigue striations in pockets of defect-free regions.

Fatigue crack growth rate has been characterized in fracture mechanics as a function of the stress intensity factor. Depending on the stress intensity factor range (ΔK), the growth rate (da/dN) measured by the crack extension (da) per fatigue cycle (dN) can be 1) no growth, if ΔK is less than a threshold value for propagation ΔK_{th}, 2) Region I growth, if ΔK is greater than ΔK_{th}, 3) Region II (steady state) growth, and 4) Region III (fast) growth, if ΔK is greater than the fracture toughness K_{IC}. The Paris-Erdogen power law for the Region II fatigue crack propagation has been used by many researchers to estimate the entire fatigue life (Refs. 2, 4, 12). However, to account for Region I fatigue crack propagation, the equation proposed by Klesnil can be used (Ref. 13)

$$N_f = \int_{a_i}^{a_f} \frac{da}{C\left(\Delta K^m - \Delta K_{th}^m\right)} \qquad (1)$$

where N_f represents fatigue life, C and m are material constants, ΔK is the stress-intensity factor range, ΔK_{th} is the threshold stress intensity factor range, and a_i and a_f are the initial and final crack lengths, respectively. The value of a_f is dependent on the fracture toughness of the material; a_i is dependent on the crack-initiating spherical or crack-like pores.

Since the present study deals with fatigue testing of specimens with preexisting defects, the stress intensity factor range ΔK may be higher than the threshold ΔK_{th}. Therefore, the fatigue propagation in the present study may have bypassed the Region I and directly entered the Region II

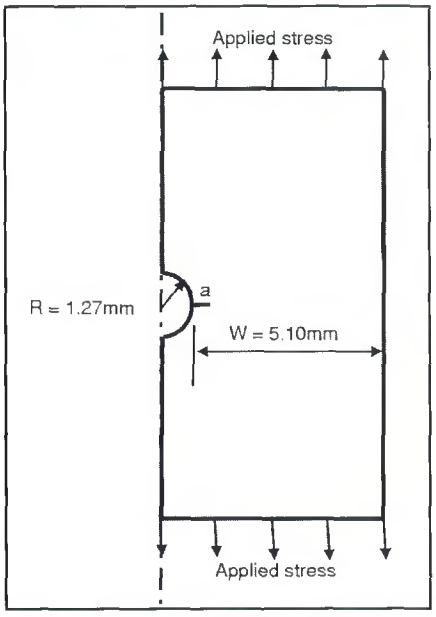

Fig. 18 — The model for stress intensity factor calculations. Due to symmetry, only half of the fatigue specimen is considered in this model.

(or steady-state) growth. While this study is not aimed at fatigue crack growth rate (da/dN), a discussion of the effect of defect size on ΔK will help understand the role of defects on fatigue life.

The stress intensity factor K_I for the defect-containing fatigue specimens was estimated for both types of pores that were exposed to the surface of the stress-concentration hole. For the specimen with multiple defects, the fatigue crack always starts from a defect that is located close to the region of maximum stress concentration and propagates along the horizontal diameter of the hole, and be perpendicular to the loading direction — Fig. 5. A model for such crack propagation is given in Fig. 18. Since the material had significant ductility, the stress intensity factor had been corrected for crack-tip plasticity using the second-order estimate. The plasticity-corrected effective stress intensity factor K_{eff} was calculated according to the following (Ref. 14):

$$K_{eff} = Y\left(a_{eff}\right)\sigma\sqrt{\pi a_{eff}} \qquad (2)$$

where $Y(a_{eff})$ was a geometrical parameter defined as

$$Y\left(a_{eff}\right) = \sqrt{\frac{W}{\pi a}}\frac{\sqrt{2\tan\frac{\pi a}{2W}}}{\cos\frac{\pi a}{2W}} \left[\begin{array}{l} 0.752 + 2.02\left(\frac{a}{W}\right) \\ + 0.37\left(1 - \sin\frac{\pi a}{2W}\right)^3 \end{array}\right] \qquad (3)$$

in which the effective crack length was $a_{eff} = a + r_y$, and the plastic zone size was estimated by

$$r_y = \frac{1}{\pi}\left(\frac{K_I}{\sigma_{YS}}\right)^2 \quad (4)$$

The peak load during fatigue tests was 108 MPa, the measured yield strength (σ_{YS}) of the material was 290 MPa, plate width (W) was 5.1 mm, crack length (a) for the average crack-like porosity was 0.4 mm, crack length (a) for the average pore depth was 0.05 mm. These values were put into the above equations and K_{eff} values were iteratively solved. The calculated maximum K_{eff} for the specimen with 0.05-mm pore exposed to the surface was 4.37 *MPa* $\sqrt{m}$; the calculated maximum K_{eff} for the specimen with 0.4-mm crack-like pores exposed to the surface was 12.79 *MPa* $\sqrt{m}$. The observed crack-like pores were estimated to produce a stress intensity factor value at about three times of that for the case of the pores. The threshold for fatigue crack propagation for cast aluminum Alloy 357 is not available, but the threshold ΔK_{th} for Alloy 356, which is similar to Alloy 357 in the present study, has been calculated by Yi et al. (Ref. 2). Their estimated threshold ΔK_{th} value is 6.1 *MPa* $\sqrt{m}$. From this, it can be suggested that a specimen with spherical pores would have a ΔK lower than the critical value for crack propagation; a specimen containing crack-like defects, however, would have a ΔK greater than the critical value for crack propagation. This analysis is qualitatively supported by the fatigue data reported in Figs. 7-11. Although this discussion only considered the peak load condition and the worst location and orientation of the defects, it did provide a quantitative insight into the relative effects of the shape and size of pores on fatigue crack initiation and propagation.

Conclusions

The major factors that decreased fatigue life for the welded specimens were the existence of welding defects. Crack-like shrinkage porosity in the welds had the most significant effect in decreasing the fatigue life of the welded specimens. Spherical pores also contributed to decreasing the fatigue life of welded specimens, although not as significant as the crack-like pores. Fatigue cracking propagated intergranularly in the welded sample, connecting the pores along its path. With increasing effects on fatigue life were mean size, area fraction, and aspect ratio of pores. Defects located near the fatigue initiation sites were more effective in decreasing the fatigue cycles. To improve fatigue cycles, elimination of crack-like defects (those with greater aspect ratios) was suggested to be more effective than decreasing the total amount of porosity, which in turn to be more effective than decreasing the average size of pores.

References

1. Evans, W. J., Lu, Z.-J., Spittle, J. A., and Devlukia, J. 1997. Fatigue crack development from defects in a cast aluminum alloy. *Proceedings of the High Cycle Fatigue of Structural Materials*, p. 445–457, TMS Fall Meeting.

2. Yi, J. Z., Gao, Y. X., Lee, P. D., Flower, H. M., and Lindley, T. C. 2003. Scatter in fatigue life due to effects of porosity in cast A356-T6 aluminum-silicon alloys. *Metallurgical and Materials Transactions* A 34(9): 1879–1890.

3. Byczynski, G. E. 2004. A study of crack initiation sites in high cycle fatigue of 319 aluminum alloy castings. JOM 56(11): 188.

4. Skallerud, B., Iveland, T., and Harkegard, G. 1993. Fatigue life assessment of aluminum alloys with casting defects. *Engineering Fracture Mechanics* 44(6): 857–874.

5. Nordmark, G. E., Herbein, W. C., Dickerson, P. B., and Montemarano, T. W. 1987. Effect of weld discontinuities on fatigue of aluminum butt joints. *Welding Journal* 66(6): 162-s to 173-s.

6. El-Soudani, S. M., and Pelloux, R. M. 1975. Anisotropy of fatigue crack propagation in aluminum alloy butt welded joints. *Welding Journal* 54(5): 144-s to 152-s.

7. Shankar, K., and Wu, W. 2002. Effect of welding and weld repair on crack propagation behaviour in aluminium alloy 5083 plates. *Materials and Design* 23(2): 201–208.

8. Matsuda, F., Nakata, K., Shimokusu, Y., Tsukamoto, K., and Arai, K. 1983. Effect of additional element on weld solidification crack susceptibility of Al-Zn-Mg alloy (report 1) Results of ring casting cracking test. *Transactions of JWRI* (Japanese Welding Research Institute) 12(1): 81–87.

9. Kearney, A. L. 1974. Avoiding cracks in weld repair of aluminum. *Foundry* 102(4): 65–67.

10. Ghosh, P. K., and Ghosh, A. K. 2004. Control of residual stresses affecting fatigue life of pulsed current gas metal-arc weld of high-strength aluminum alloy. *Metallurgical and Materials Transactions* A 35A(8): 2439–2444.

11. Bertini, L., Fontanari, V., and Straffelini, G. 1998. Influence of postweld treatments on the fatigue behavior of Al-alloy welded joints. *International Journal of Fatigue* 20(10): 749–755.

12. Wang, Q. G., Apelian, D., and Lados, D. A. 2001. Fatigue behavior of A356-T6 aluminum cast alloys. Part 1. Effect of casting defects. *Journal of Light Metals* 1(1): 73–84.

13. Klesnil, M., and Lukas, P. 1972. Influence of strength and stress history on growth and stabilization of fatigue cracks. *Engineering Fracture Mechanics, Vol.* 4, pp. 77–92.

14. Anderson, T. L. 2005. *Fracture Mechanics — Fundamentals and Applications*, 3rd Edition, p. 52, Taylor & Francis.